Journal of Materials Chemistry A

ROYAL SOCIETY OF CHEMISTRY

PAPER

View Article Online
View Journal | View Issue

Cite this: J. Mater. Chem. A, 2024, 12, 5194

Deciphering the role of Fe impurities in the electrolyte boosting the OER activity of $LaNiO_3$†

Haritha Cheraparambil,[a] Miquel Vega-Paredes,[b] Yue Wang,[a] Harun Tüysüz,[a] Christina Scheu[b] and Claudia Weidenthaler *[a]

Received 3rd November 2023
Accepted 20th January 2024

DOI: 10.1039/d3ta06733e

rsc.li/materials-a

Perovskites have emerged as potential catalysts for the alkaline oxygen evolution reaction. Iron impurities in the electrolyte play an important role in enhancing the catalytic activity of Ni centres, but the nature of active sites is elusive. In this article, we report a detailed study of iron incorporation dynamics and provide direct spectroscopic evidence for surface re-construction and dynamic active site evolution in $LaNiO_3$ perovskite using identical location scanning transmission electron microscopy, electron energy loss spectroscopy and *in situ* electrochemical Raman spectroscopy. We demonstrate that the electrocatalytic activity is enhanced up to an amount of 7.5 ppm Fe traces in the electrolyte by lowering the Tafel slope from 115 to 49 mV dec^{-1}. The iron impurities in the electrolyte enter the perovskite structure, leading to the dissolution of the A-site, vacancy formation, and amorphization of surface layers. The origin of activity arises from these amorphous layers which are ~5 nm thick and rich in Ni oxyhydroxides, Fe oxyhydroxides, and a Ni–O–Fe coordinated environment. Together with pH-dependent studies, we confirm the lattice oxygen mechanism in the presence of Fe impurities. Our work provides new insights into the design and a deeper understanding of Ni–Fe synergetics in perovskite-based catalysts for alkaline OER.

Introduction

Electrochemical water splitting is an effective way to produce green hydrogen and has led to tremendous research efforts in the pursuit of carbon neutrality and sustainable energy production. Nevertheless, the overpotential of the process is high due to the sluggish kinetics of the anodic four-electron transfer oxygen evolution reaction (OER).[1–3] Therefore, the development of an active, stable, and cost-effective OER catalyst is necessary. Even though the state-of-the-art catalysts, Ru- and Ir-based oxides, exhibit excellent OER performance, the scarcity and high costs impede their practical applications.[4,5] Therefore, much of the ongoing research is focused on the preparation of alternative low-cost and highly active catalysts, of which transition-metal oxides such as perovskites (ABO_3) have gained attention due to their mixed ionic–electronic conductivities, as well as structural and chemical tunability. By substituting the A or B site, perovskites can form myriad structures that can indirectly modulate physical, chemical, and catalytic properties.[6–8]

Significant progress has been made in the rational design of perovskites by tailoring the valence, defects, and morphology to increase the number of accessible active sites.[9–11] Numerous studies also direct towards surface reconstruction, stability, and degradation of the perovskite catalysts during OER.[12–15] Most of the perovskites are identified to undergo a concerted electron–proton transfer, also known as the adsorbate evolution mechanism (AEM).[6] Recently, this has been challenged by an alternate pathway known as the lattice oxygen mechanism (LOM), in which lattice oxygen from the oxides is also involved in the formation of O_2, enhancing OER performance.[16–18] It has also been shown that traces of Fe impurities from the electrolyte significantly enhance the OER performance of Ni-based oxides and perovskites.[19–23]

Despite these intensive studies, there remains a lot of ambiguity and unanswered questions on the iron incorporation dynamics of perovskite oxides. The extent to which Fe impurity from the electrolyte can enhance the OER activity and how it alters the surface layers of the catalyst are still unclear. It is important to study the surface alterations on atomic and local scales because such surface changes could result in the evolution of dynamic species that are different from the bulk nature of perovskite oxides.[24] While the true nature of active sites in hydr(oxy)oxides is still under discussion,[22,25–27] the structural complexity of perovskites makes it even harder to probe the short-lived dynamic species. In such instances, it is crucial to combine the observations from both *in situ*/*operando* and *ex situ*

[a]Max-Planck-Institut für Kohlenforschung, Kaiser-Wilhelm-Platz 1, D-45470 Mülheim an der Ruhr, Germany. E-mail: weidenthaler@mpi-muelheim.mpg.de
[b]Max-Planck-Institut für Eisenforschung, Max-Planck-Straße 1, D-40237 Düsseldorf, Germany

† Electronic supplementary information (ESI) available. See DOI: https://doi.org/10.1039/d3ta06733e

experiments to establish functional links between the surface reconstruction, and the catalytic mechanism.

Herein, we report a holistic study on lanthanum nickelate perovskite to understand the complex electrode–electrolyte interface at atomic and local scales. Systematic investigation of the effects of electrolyte impurities on the catalyst performance has shown that the presence of iron impurities enhances the electrocatalytic performance to some extent and has adverse effects beyond that. Using *in situ* electrochemical Raman spectroscopy, electron energy loss spectroscopy (EELS), and identical location scanning transmission electron microscopy (IL-STEM) reveals that the interplay between catalytically and dynamically evolving NiOOH and active Fe species from the electrolyte is crucial in favouring the LOM pathway. The studies establish functional links between the perovskite properties, the influence of electrolyte impurities, surface evolution, and the reaction mechanism.

Experimental section

Synthesis

Different perovskites were synthesized *via* the solution combustion method followed by calcination. In a typical reaction, stoichiometric amounts of nitrates [$La(NO_3)_3 \cdot 6H_2O$ Alfa Aesar, CAS 10277-43-7, purity 99.99%, $Ni(NO_3)_2 \cdot 6H_2O$ Alfa Aesar, CAS 13478-00-7, purity $\geq$ 97%] were dissolved in water. Glycerol (Sigma-Aldrich, CAS 56-81-5) was added as the fuel in an equal molar ratio concerning the metal nitrates. The mixture was stirred for 15 min on a magnetic stirrer and 3 mL nitric acid was added dropwise. The mixture was heated to 250 °C until the solvent was completely evaporated and an auto-combustion reaction took place. This resulted in the formation of a sponge-like powder which was further used as the precursor. The precursor was further calcined at 700 °C for 30 min to obtain the perovskite phase.

Characterization

X-ray powder diffraction (XRPD). XRPD experiments were performed on a PANalytical X'Pert Pro diffractometer working with Cu K$\alpha_{1,2}$ radiation ($\lambda = 1.5406$ Å). The data were collected in Bragg–Brentano geometry with a Ni-filter in the secondary beam path and an X'Celerator real-time multi-strip position sensitive detector (PSD) in the 2θ range of 10–85°. All XRPD patterns were analyzed with the DiffracSuite Topas V6 software (Bruker AXS GmbH, Karlsruhe, Germany).[28] The crystallite sizes for the perovskite nanoparticles, reported as column length distributions, were evaluated with the whole powder pattern modelling approach implemented in TOPAS V6.[29,30]

X-ray total scattering data. Total scattering experiments were performed at the beamline P02.1 at PETRA III, Deutsches Elektronen-Synchrotron (DESY) [energy: 60 keV ($\lambda = 0.20723$ Å)]. For data collection, a Varex XRD 4343DT detector (150 × 150 μm^2 pixel size; 2880 × 2880 pixel area) was used. Data were collected at RT and the measurement time per frame was 10 min. Data were further evaluated by pair distribution function (PDF) analysis using PDFgetX3 (ref. 31) within the package xPDFsuite.[32] The Q_{damp} (0.027 $Å^{-1}$) and Q_{broad} (0.003 $Å^{-1}$) were determined with a silicon standard.

Scanning transmission electron microscopy (STEM). The micrographs were acquired in a probe-corrected Titan Themis microscope (Thermo Fisher Scientific) operated at 300 kV. A 100 mm camera length was used, which resulted in a collection angle of 78–200 mrad for the high angle annular dark field (HAADF) and of 18–73 mrad for the annular dark field (ADF). Energy dispersive X-ray spectroscopy (EDS) and electron energy loss spectroscopy (EELS) spectral images were acquired in the same microscope. For the EELS experiments, a dispersion of 0.250 eV per channel and a pixel acquisition time of 1 second were used.

In identical location IL-STEM, the same region of the sample can be studied before and after an electrocatalytic reaction, and has been used for determining degradation mechanisms[33,34] and the nature of active species[35] of nanocatalysts. For the IL experiments, a 10 μL drop of a 0.3 mg mL^{-1} dispersion of $LaNiO_3$ on deionized water was drop-cast on a hole carbon-coated Au TEM finder grid (Plano). After the initial characterization by STEM, the $LaNiO_3$-containing grid was used as a working electrode in a three-electrode set-up. A Pt wire (Redoxme) and a reversible hydrogen electrode (Gaskatel) were used as counter and reference electrodes, respectively. For making electrical contact between the grid and the potentiostat instead of the classical glassy carbon–Teflon cap approach, a gold thread was used to avoid loss of current created by the evolved gas bubbles.

Nitrogen physisorption. The measurements were carried out using the 3Flex Micromeritics instrument at 77 K and the Brunauer–Emmett–Teller (BET) surface area was calculated from the relative pressure range (p/p^0) between 0.07 and 0.2. Prior to the measurements, the powder samples were degassed under a vacuum at 120 °C for 10 h.

Electrochemistry. All electrochemical measurements were performed in a three-electrode Teflon cell with a rotating disc electrode (Model: AFMSRCE, PINE Research Instrumentation), a reversible hydrogen electrode (HydroFlex, Gaskatel) as the reference, and a Pt wire as the counter electrode. 1 M KOH was used as the electrolyte unless specified. The temperature of the cell was maintained at 25 °C by a water circulation system. Prior to the measurements, the electrolyte was purged with argon to remove the dissolved oxygen. For the preparation of the working electrodes glassy carbon (PINE, 5 mm diameter, 0.196 cm^2 area) electrodes were polished with alumina suspension (5 and 0.25 μm, Allied High Tech Products, Inc.). They were further washed in deionized water (DI) by sonicating it for 5 min. The catalyst ink was prepared by dispersing 4.8 mg of sample powder in 1 mL mixed solution of DI water : isopropanol (1 : 1) and 50 μL Nafion 117 (Sigma-Aldrich) binder and further sonicating for 30 min to form a homogeneous ink. 5.25 μL of catalyst ink (catalyst loading of 0.12 mg cm^{-2}) was drop cast onto the polished glassy carbon electrode and dried under argon atmosphere overnight. Cyclic voltammetry (CV) was performed at a scan rate of 50 mV s^{-1} within the 0.7 to 1.6 V *vs.* RHE potential window. Linear scan voltammetry (LSV) was measured after stabilizing the surface *via* CV in a potential window of 0.7 to

1.7 V *vs.* RHE at a scan rate of 10 mV s^{-1}. Chronopotentiometry was performed at 10 mA cm^{-2} of geometric current density in 1 M KOH with 7.5 ppm Fe content to test the stability of the catalyst. Electrochemical impedance spectroscopy (EIS) was measured at 1.66 V *vs.* RHE and 5 mV of amplitude within the 100 mHz to 100 kHz frequency range and the obtained Nyquist plots were then fitted to the equivalent circuit model using the EC-Lab software. The IR drop was compensated at 85%.

Raman spectroscopy. The spectra were collected with an inVia Renishaw Raman microscope equipped with a laser excitation of 532 nm, 1800 L mm^{-1} grading, and coupled with a 50× objective lens (Leica). *In situ* Raman measurements were carried out in a custom-designed *in situ* electrochemical flow cell. Au substrate was polished and roughened following the previously reported protocol[36] and the sample ink solution was drop cast onto it. Pt wire and RHE were used as the counter and reference electrodes respectively. Argon-saturated 0.1 M KOH was used as the electrolyte and the flux was controlled using a peristaltic pump with a flow rate of 1–8 mL min^{-1} to remove the bubble formation. The measurements were performed in purified KOH and purified KOH with 7.5 ppm Fe impurities for comparison.

Inductively coupled plasma-optical emission spectrometry (ICP-OES). The measurements were carried out with a SPECTROGREEN instrument, and the electrolyte solution samples were taken from the electrochemical cell before and after the reaction.

Results and discussion

Simple perovskite, $LaNiO_3$ was synthesized by an optimized solution combustion method followed by calcination.[37] Glycerol was used as the fuel, and the self-combustion occurred at 250 °C, resulting in the formation of spongy black precursors. A phase pure sample is obtained at 700 °C, as confirmed by Rietveld analysis (Fig. 1a). The compound crystallizes in a rhombohedral structure (space group $R\bar{3}c$). The column length distribution was determined using the whole powder pattern modeling (WPPM) approach assuming spherical crystallites with a lognormal distribution of their column length.[29] The volume-weighted crystallite size (LVol) was calculated to be 6–8 nm (Fig. S1†). Detailed analysis of the refined data reveals an asymmetric broadening of the reflections at 23° and 40° 2θ. In addition, the calculation of the Fourier difference map reveals the presence of residual electron density around the A site (La) in the direction of the *c*-axis and around the B site (Ni) around the *a*–*b* plane as depicted in Fig. 1b.

To gain more information on the local structure, total scattering experiments were performed and the resulting PDFs were analyzed as shown in Fig. 2a. Total X-ray scattering data and subsequent pair distribution function (PDF) analysis have proven to be powerful tools for characterizing amorphous, distorted and crystalline structures not only in the short-range but also in the intermediate and long ranges.[38,39] The phase crystallizes in a rhombohedral structure with space group $R\bar{3}c$. In a perfect crystal system, the first pair correlation corresponds to the Ni–O distances in the NiO_6 polyhedron which appears at 1.94 Å as shown in (i), and the next pair correlation is assigned to the La–O distances in a 9-fold coordinated polyhedron (ii). There are three shorter (2.43 Å) and six longer (2.71 Å) La–O bond lengths which result in a broadening of the pair correlation. However, in the present perovskite structure, the NiO_6 polyhedra have shorter Ni–O bond lengths (1.85 Å) and La–O polyhedra have longer bond lengths (2.48 Å and 2.83 Å). These observations indicate the presence of disorder. The pair correlation at 3.8 Å (iii) includes contributions from the Ni–Ni distances and La–La distances in corner-sharing Ni–O and La–O polyhedra. La–O polyhedra share edges as well, where the La–La distances appear around 5.4 Å.

Scanning electron microscopy (SEM) shows the surface topology of the sample (Fig. S2a and b†). The particles are densely packed with interparticle porosity and the BET surface area from physisorption experiments was calculated to be 10 m^2 g^{-1} (Fig. S3†). Scanning transmission electron microscopy (STEM) probes the crystallinity of the material. It confirms the presence of stacking faults, as shown in Fig. 3a in the annular dark field (ADF) and Fig. 3b in the high-angle annular dark field (HAADF) images. This agrees well with the observations obtained from the Fourier difference map as well as from PDF analysis.

Fe-dependent electrochemical performance

Once the structure of the catalyst was determined, the catalytic OER activity of the system was tested according to the adapted

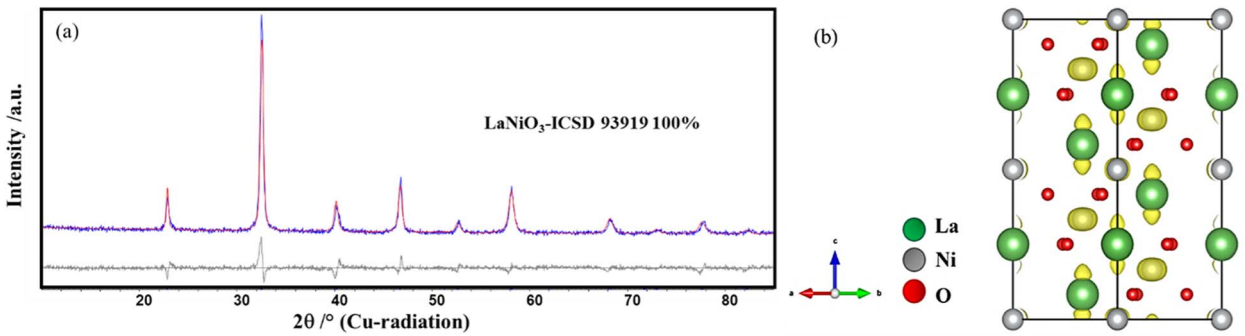

Fig. 1 (a) Rietveld refinement plot of $LaNiO_3$ obtained at 700 °C. (b) Fourier difference map showing the residual electron density (yellow in colour).

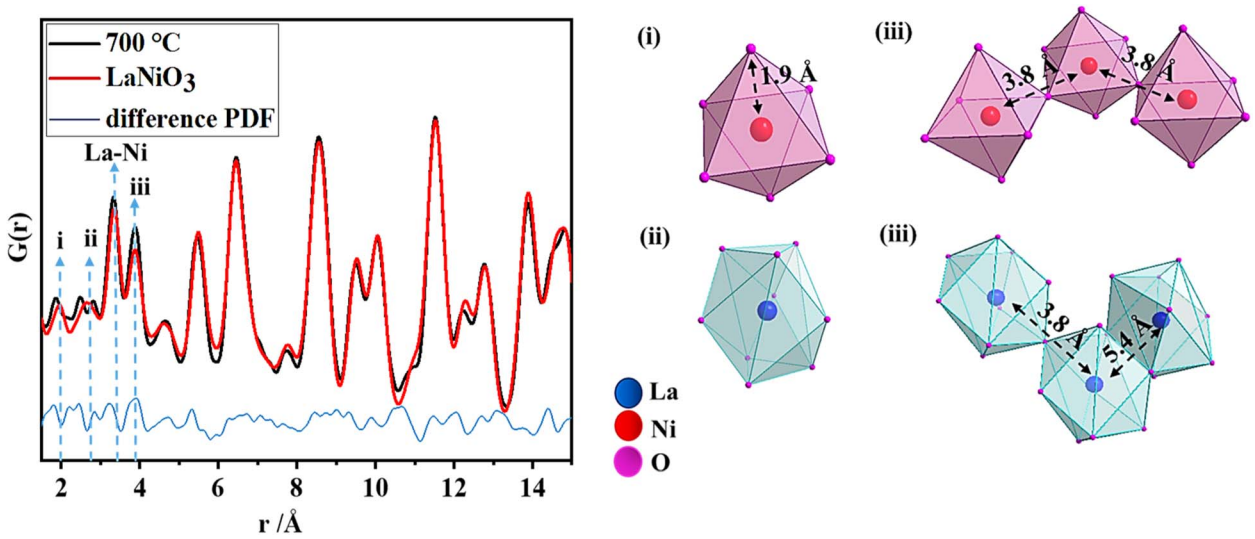

Fig. 2 PDF refinement of $LaNiO_3$ obtained at 700 °C, with the explanation of the nearest pair correlations (i–iii).

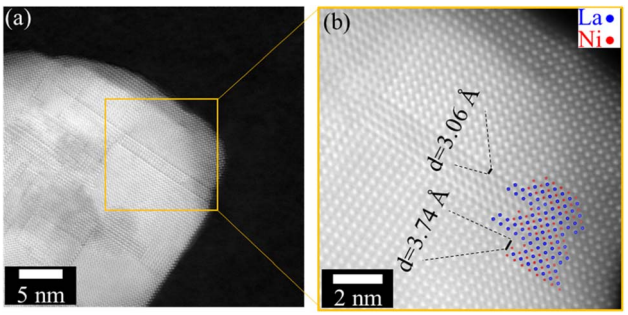

Fig. 3 (a) ADF image of $LaNiO_3$, showing the presence of multiple planar defects. (b) High-resolution HAADF-STEM micrograph. The positions of the La (blue) and Ni (red) columns are indicated.

protocol proposed by Jaramillo and co-workers.[40] The electrocatalysts can undergo various surface reconstructions in the presence of iron in the electrolyte.[19,20] To systematically study the role of Fe, the electrolyte was first purified as reported in the literature.[22,41] The iron concentration in the electrolyte was varied from 1 ppm to 10 ppm by the controlled addition of iron nitrate nonahydrate as the iron source. The concentration of Fe was further confirmed by inductively coupled plasma optical emission spectroscopy (ICP-OES) (Table S1†). As the Fe content in the electrolyte increases, the area under the redox peaks increases indicating that more Ni centres are getting activated (Fig. 4a). Along with the significant increase in the activation of the catalyst, there is also a shift in the redox behaviour corresponding to the electronic interaction between Fe and Ni centres, as shown in the inset of Fig. 4a.[22,42] No redox behaviour of iron was observed because the oxidation of metallic Fe to Fe^{2+}/Fe^{3+} oxides or hydroxides occurs in the potential range from −360 mV to −1.0 V *vs.* the reversible hydrogen electrode (RHE). This observation is also consistent with literature reports.[43] However, the OER activity increases up to a maximum Fe content of 7.5 ppm in the electrolyte and then slowly decreases as shown in Fig. 4b. Even though iron species increase the activity of Ni centres, an excess amount can aggravate the charge transfer to water because of the insulating property of iron oxyhydroxides.[41,42] Fig. 4b and d show that the catalyst can deliver a maximum current density of 340 mA cm^{-2} with an overpotential of 300 mV *vs.* RHE, thus boosting the overall activity. The reaction kinetics are further analyzed using Tafel plots, which confirm the excellent performance of $LaNiO_3$ in the presence of traces of Fe impurities, lowering the Tafel slope from 115 to 49 mV dec^{-1} as illustrated in Fig. 4c.

Complementary electrochemical impedance spectroscopy (EIS) was used to probe the charge transfer behaviour in the presence of Fe impurities in the electrolyte. Fig. 4e depicts the Nyquist plots from which the charge transfer resistance was calculated using a simplified Randles model $(R_\Omega)(R_{ct}Q_{dl})$ as shown in the inset of Fig. 4e. The results are summarized in Table S2.† A significant decrease of the charge transfer resistance (R_{ct}) in the presence of Fe impurities is observed for $LaNiO_3$. This denotes the synergistic effects between Fe and the Ni centres that facilitate charge transfer. However, the R_{ct} is lowest at a Fe concentration of 7.5 ppm in KOH, and at higher Fe concentrations, R_{ct} increases, also indicating that the excess of Fe hinders the conductivity.

The chronopotentiometry (CP) measurements were performed on the catalyst in 1 M KOH with 7.5 ppm Fe impurities. This sample retains the activity at 10 mA cm^{-2} for up to 12 h (Fig. 4f). The high stability is also confirmed by the subsequently obtained TEM image, showing that the crystallinity is preserved (Fig. S4†).

Studying the surface reconstruction using IL-STEM

IL-STEM was used to follow the changes of the same particles on the atomic scale before and after the electrochemical cycles. After cycling $LaNiO_3$ in 1 M KOH with Fe impurity (7.5 ppm), an amorphization of the surface is observed, while the crystallinity of $LaNiO_3$ is preserved when cycled without Fe impurities

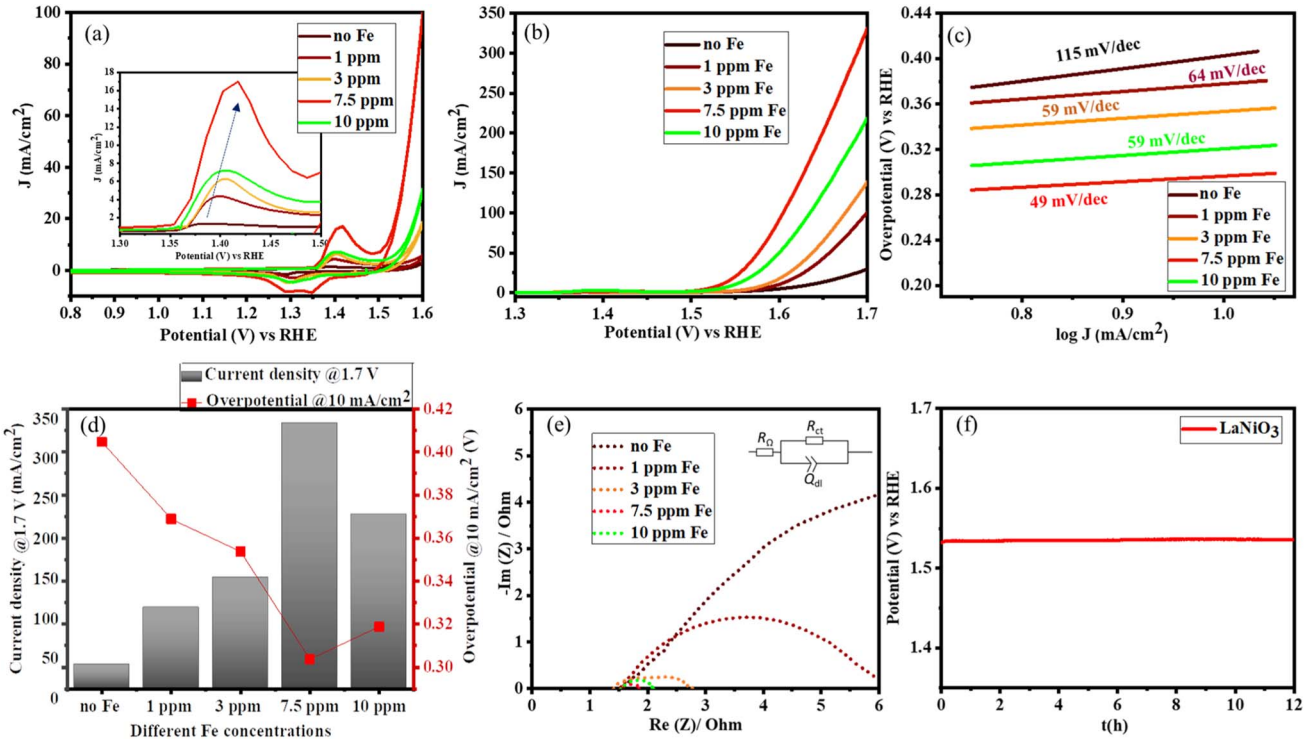

Fig. 4 (a) Cyclic voltammetry after 50 cycles. The inset shows the shift in the oxidation peak of Ni in the presence of different Fe contents. (b) Linear sweep voltammetry (LSV) after 100 cycles of CV (c) Tafel plots (d) overview on the overpotential at 10 mA cm^{-2} and current density at 1.7 V *vs.* RHE (e) Nyquist plots from EIS measurements at 1.66 V *vs.* RHE on $LaNiO_3$ in different concentrations of Fe in the electrolyte (1 M KOH) and (f) chronopotentiometry on $LaNiO_3$ at 10 mA cm^{-2} for 12 h in 1 M KOH with 7.5 ppm of Fe impurity.

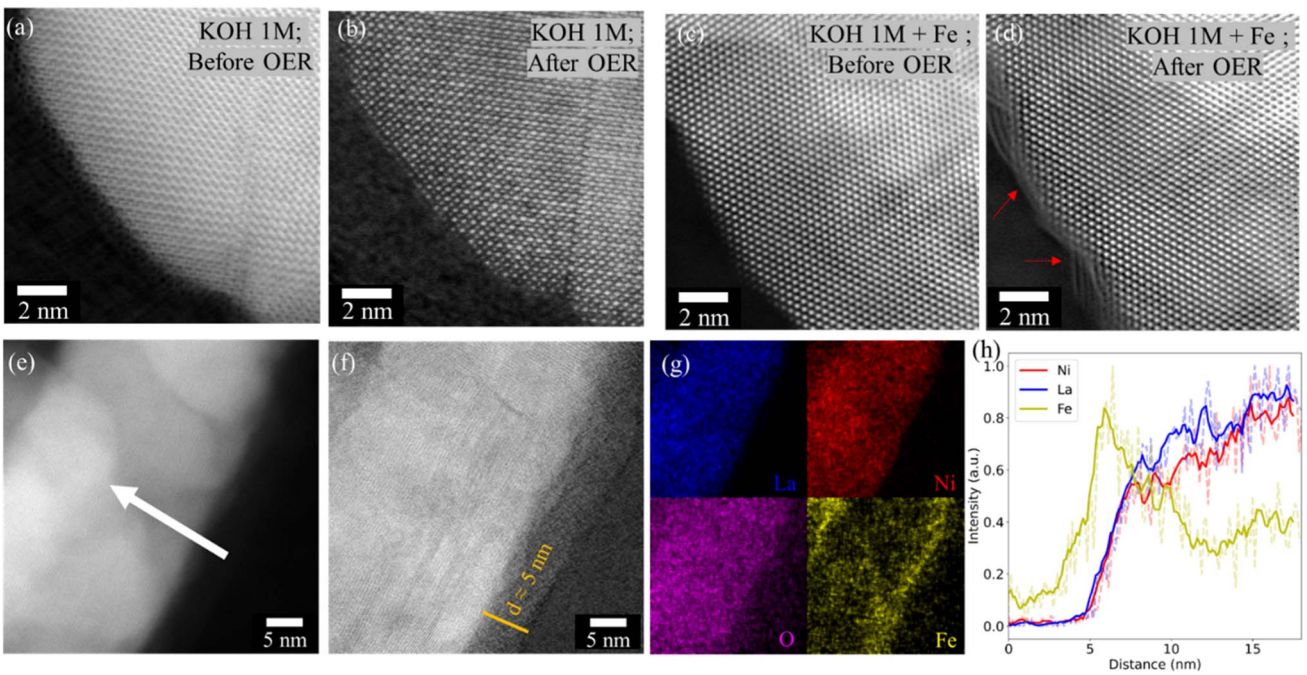

Fig. 5 Identical location ADF-STEM micrographs of $LaNiO_3$ (a) before, (b) after OER in 1 M KOH, (c) before, and (d) after OER in 1 M KOH with Fe impurities. When Fe impurities are added to the electrolyte, an amorphous layer is formed (indicated by the red arrows in (d)). The structure and composition of the amorphous (oxy)hydroxide layer formed during OER are analyzed with (e) HAADF STEM (f) ADF STEM and (g) EDS composition maps. Corresponding intensity profiles (h) along the direction indicated by the arrow in (e) of a $LaNiO_3$ cycled in 1 M KOH with Fe impurities.

(Fig. 5a–d). The amorphous layer was further studied as shown in Fig. 5e–h. STEM imaging and EDS analysis revealed that the Fe species are localized in the newly formed amorphous surface with a thickness of about 5 nm.

Identifying the nature of active sites

In situ Raman studies were performed to follow the structure reconstruction and the evolution of active species during OER. The vibration modes of $LaNiO_3$ are presented in Table S3.† The characteristic band around 400 cm^{-1} corresponds to the vibrational modes of the NiO_6 polyhedra.[44] Once the catalyst contacts the KOH electrolyte, the band around 800 cm^{-1} appears, corresponding to the adsorbed hydroxide/oxyhydroxide species on the Au substrate.[36,45] This band is observed in both samples and is very prominent during the onset of OER.

In situ Raman spectra collected during changing potentials in purified KOH are shown in Fig. 6a. The vibrational mode at 400 cm^{-1} is preserved at all potentials, although its intensity decreases with the increase in the applied potentials. At a potential of 1.0 V, a broad Raman band appears between 450 cm^{-1} and 600 cm^{-1}, which resolves into two separate bands at 1.3 V centred around 474 cm^{-1} and 555 cm^{-1}. They correspond to the bending and stretching vibration modes of Ni–O in Ni-oxyhydroxide species. Due to resonance effects, these two vibrational modes are known to have a high Raman cross-section. From the relative intensities of the two bands ($I_{E_g}/I_{A_{1g}}$ = 1.15), they are attributed to the presence of γ-NiOOH.[46]

The *in situ* Raman spectra of $LaNiO_3$ measured in the presence of Fe impurities are shown in Fig. 6b. The vibrational mode around 800 cm^{-1} is also observed here and becomes sharper at potentials between 1.35 and 1.45 V where Ni exhibits its classic redox behaviour (Ni^{3+} to Ni^{4+}). When the potentials are applied, the vibrational mode at 400 cm^{-1} gradually disappears, hinting at surface distortion. The bands disappear completely around 1.45 V indicating local amorphization of the structure during OER in the presence of Fe. In addition, the broad Raman bands around 900–1150 cm^{-1} observed at

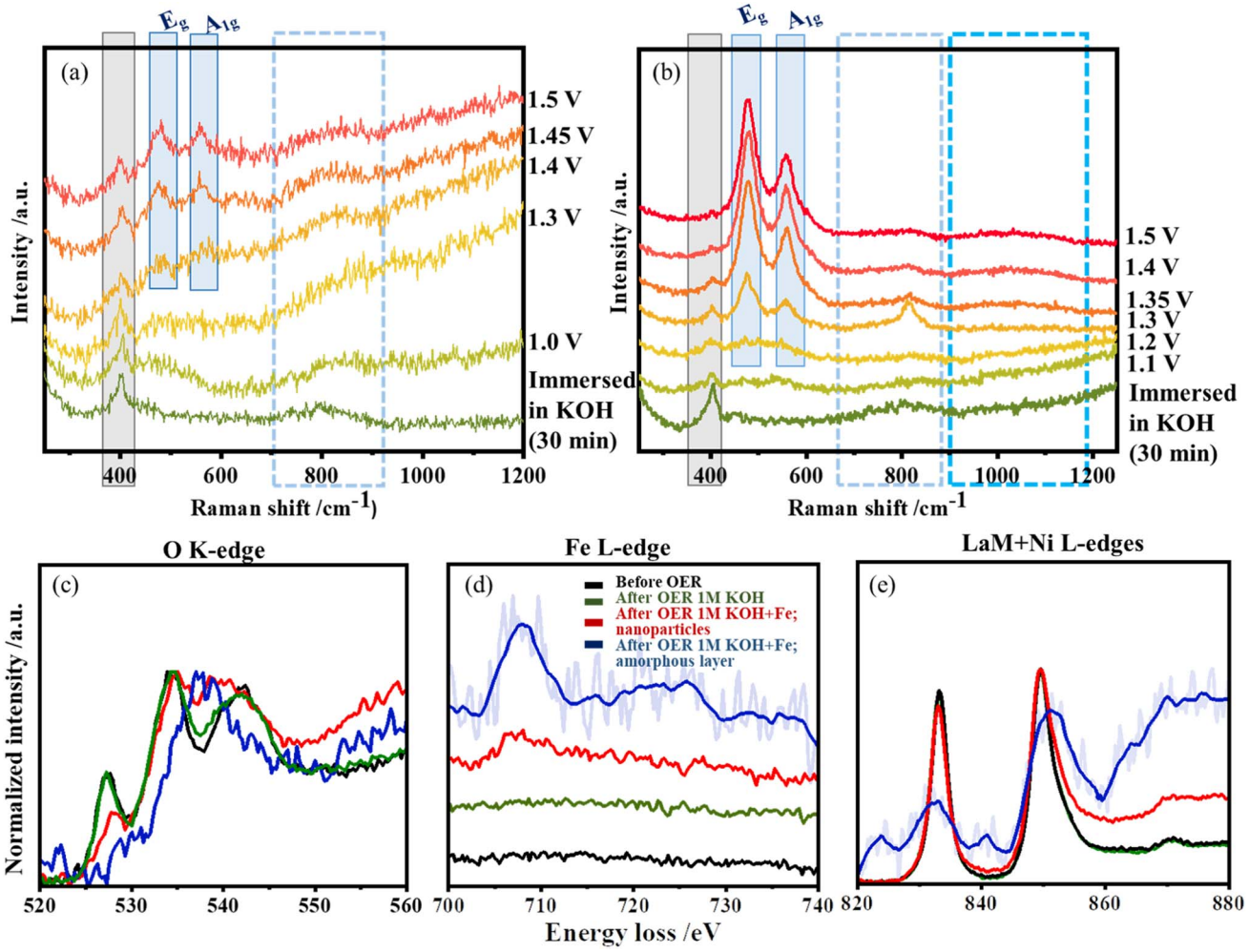

Fig. 6 (a) *In situ* Raman spectra of $LaNiO_3$ collected during the OER process (1.0–1.7 V *vs.* RHE) in 1 M purified KOH, (b) with the addition of Fe impurities. Comparison of EELS spectra collected for $LaNiO_3$ in different conditions: before OER (black colour), after OER in 1 M purified KOH (green colour), nanoparticles after OER in 1 M KOH with Fe impurities (red colour), and amorphous layer (blue colour) formed after OER in 1 M KOH with Fe impurities. The energy loss region of the (c) O K-edge, (d) Fe L-edge, and (e) La M + Ni-L edge are shown.

potentials above 1.35 V, the region for Ni redox behaviour and onset of OER, are attributed to the formation of the active oxygen/superoxide species.[47] The most dramatic effect of the Fe impurities is the early formation and change in absolute and relative intensities of the pair of NiOOH bands; both bands (E_g and A_{1g}) are more intense and the relative intensity ($I_{E_g}/I_{A_{1g}} = 1.41$) increases with Fe incorporation, as shown in Fig. S5.† The high Raman cross-section of the NiOOH vibrations limits the amount of information that can be extracted from the Fe contribution with low Fe contents.[19]

The *in situ* Raman data were complemented by EELS experiments, which provide higher spatial resolution. HAADF-STEM micrographs of the areas where the EELS spectra were collected are provided in Fig. S6.† An amorphous layer is observed only when the electrolyte contains Fe impurities during OER, which is in good agreement with the IL STEM and Raman spectroscopy observations. Fig. 6c shows the O K-edge. It exhibits three prominent peaks: a pre-peak located around 527 eV related to electronic transitions from O 1s to O 2p orbitals hybridized with Ni 3d, followed by peaks around 534 eV and 540 eV corresponding to the long-range order of the crystal, as well as the density of La 5d and Ni 4s–O bond.[35,48,49] The pre-peak changes significantly after OER in the presence of Fe impurities, and the intensity of the O K-edge pre-peak at ~527 eV is reduced. This indicates that the local coordination and the valence state have changed and that lattice oxygen most likely takes part in the catalysis.[35,49] For the amorphous layer, the main peak is shifted to higher energy losses and is at 540 eV. This could indicate the formation of Fe^{3+} species[50] or Ni–O–Fe species since the O-K edges of α- and β-FeOOH and Ni-oxyhydroxide have similar features.[51] Only minor changes in the O-K edge are observed for the system after OER in purified KOH.

The La M4,5 and Ni L2,3 edges are known as white lines, and their position and relative intensity value are known to be affected by the oxidation state of the element. The white lines are visible in Fig. 6e and appear for La M5 at an energy loss of 832 eV, while La M4 appears at 849 eV. For Ni, the white lines L3 and L2 possess energy losses of 852 eV and 872 eV. Due to the overlap between the La M4 and the Ni L3 white lines, the interpretation of the data is difficult, but some changes can be observed for the different samples. In the nanoparticle region measured after OER in the presence of Fe impurities, the intensity of the La M5 at 832 eV decreases compared to the M4 edge, but there is no shift in the edge position. This indicates that the oxidation state of La does not change and the La concentration decreases relative to Ni. This is also confirmed by ICP-OES measurements of the electrolyte after OER on $LaNiO_3$ in the presence of Fe impurities where we detect La (0.04 ppm) dissolved into the electrolyte as shown in Table S4.† Since the peak at ~850 eV contains white line contributions of La M4 and Ni L3, increasing the relative Ni concentration leads to a higher relative intensity of this peak. Similarly, the amorphous layer present after OER in KOH + Fe is also enriched in Ni. The L2,3-edges are caused by electronic excitations from 2p core levels to unoccupied 3d orbitals. This is directly reflected in the 3d electronic states and therefore provides information about the valence state. The peak of the La M4/Ni L3 white line is broadened and shifted to higher energy losses for the amorphous layer. In a first approximation, as the La M5 white line remains at the same energy loss, it is assumed that both are related to a change in the Ni ions. Accordingly, the shift of the Ni L3 white line to higher energy losses in the presence of Fe indicates that Fe promotes and stabilizes higher oxidation states of Ni.[52] The broadness of the peaks shows the presence of different oxidation states.[53]

The Fe L-edge as shown in Fig. 6d displays a very broad peak centred around 708 eV, which becomes very prominent after OER in the presence of Fe impurities in the amorphous layer compared to the nanoparticle region. This is an indication that the amorphous layer is rich in Fe, complementing the EDS observations. The ICP-OES (Table S4†) data shows the reduction of the Fe content in the electrolyte before and after OER. It also confirms that Fe has entered the interface. The broad features could again indicate the presence of amorphous or disordered Fe oxyhydroxides or direct towards a mixed coordination environment with Ni. These observations are consistent with O K-edge and Ni L2,3-edges.

These results show that the origin of activity in $LaNiO_3$ catalyst arises from NiOOH which interacts with Fe species from the electrolyte. This interaction leads to the dissolution of lanthanum and, the formation of oxygen vacancies, which subsequently result in the formation of amorphous and dynamically active oxyhydroxide layers of *ca.* 5 nm thick. The amorphous layers are identified to be a mixture of Ni-oxyhydroxides, Fe-oxyhydroxides, and a Ni–O–Fe coordinated environment. The presence of Fe not only promotes and stabilizes the higher oxidation state of Ni but also could act as a potential catalytic site.

Elucidating the OER reaction mechanism using pH-dependent studies

In addition, it was studied how the OER activity can be adjusted by varying the pH value. This affects the free energy of adsorbed intermediates, the concentration of OH^-, or the surface coverage of the adsorbed *OH and *OOH intermediates.[54] From theoretical calculations and O-isotope experiments on Sr-based perovskites, it was discussed that the pH-dependent OER activity experiments indicate the lattice oxygen mechanism.[54,55] The OER activities of $LaNiO_3$ were measured in alkaline electrolytes of different pH with (7.5 ppm Fe) and without Fe impurities. A high-purity semiconductor-grade KOH was used as the electrolyte.

Cyclic voltammetry measurements show that the surface is activated with increasing pH, whether Fe impurities are present or not but the activation is pronounced in the presence of electrolyte impurities. However, the current density increases tenfold in the presence of Fe impurities (Fig. 7a), while the activation is boosted only threefold in the absence of Fe impurities (Fig. 7b) as the pH of the electrolyte increases from 12.5 to 14. A similar trend is observed for the OER overpotential in electrolytes with different pH values as summarized in Fig. 7c. Thus, both cyclic voltammetry and linear sweep

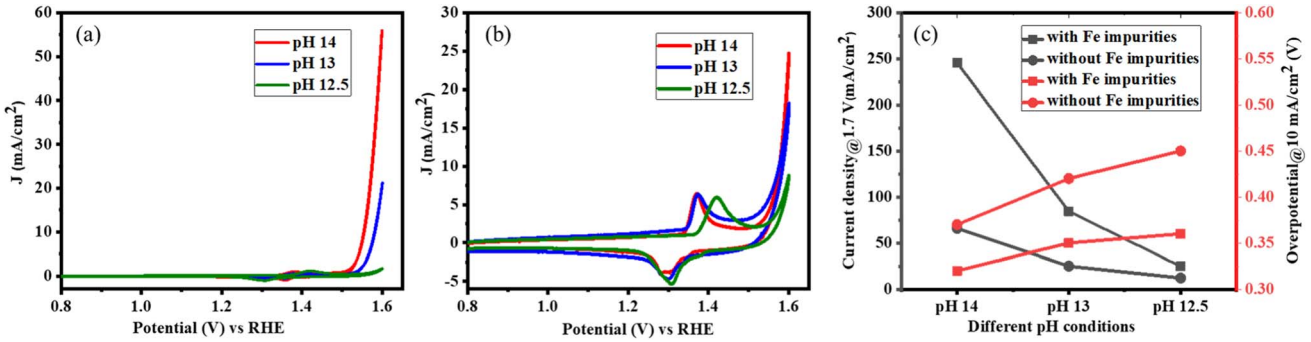

Fig. 7 Cyclic voltammetry data after the 50th cycle was obtained for $LaNiO_3$ under different pH conditions: (a) with Fe impurities, (b) without Fe impurities, (c) overview of the overpotential at 10 mA cm^{-2} and current density at 1.7 V *vs.* RHE at different pH conditions with and without Fe impurities in the electrolyte.

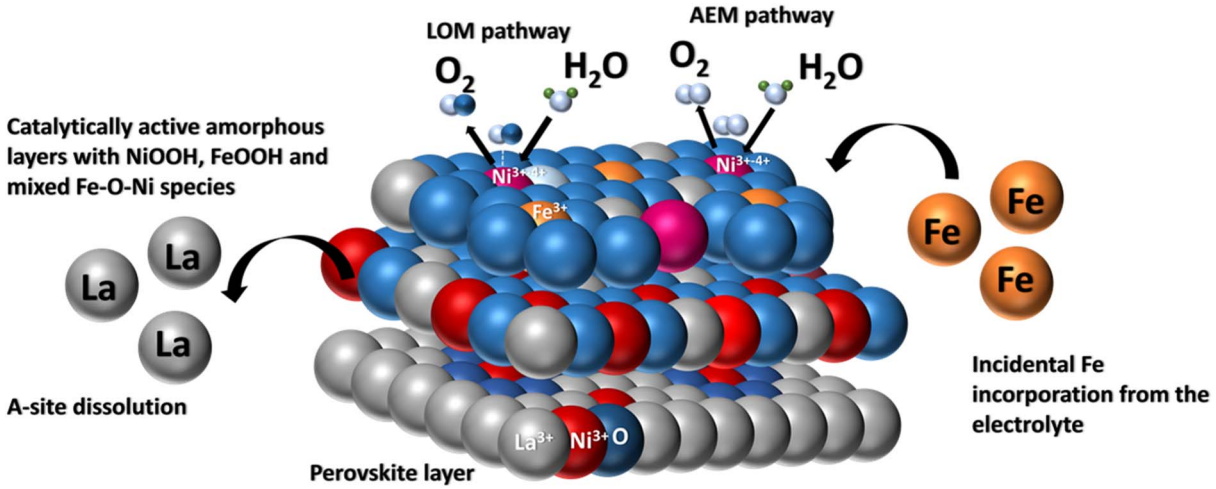

Fig. 8 Pictorial representation of incidental Fe incorporation dynamics on a $LaNiO_3$ system during OER.

voltammetry measurements show that the OER kinetics of $LaNiO_3$ is pH-dependent and the dependence is particularly pronounced in the presence of Fe impurities, which increase the overall performance *via* the lattice oxygen mechanism.

As Fig. 8 depicts, when $LaNiO_3$ comes in contact with the electrolyte, an electrochemical interface is established where the active Fe species interact with the perovskite surface resulting in surface alteration which includes La dissolution, formation of oxygen vacancies and the formation of an amorphous layer. However, the rate of ion dissolution and redeposition reaches an equilibrium state[25] and establishes a stable interface over longer cycles. Additionally, the stable dynamic interface offers two active sites for OER, promoting the O_2 production rate *via* the lattice oxygen mechanism.

Conclusions

In summary, a combination of controlled perovskite synthesis, detailed structure analysis, atomic scale microscopy imaging, EELS, and *in situ* Raman spectroscopy demonstrated how the catalyst surface evolves and forms dynamic active sites during OER in the presence of Fe impurities in the electrolyte. Fe impurities in the electrolyte have been shown to favour the kinetics to some extent and, moreover, can hinder the OER activity of the catalyst. The Fe species from the electrolyte lead to significant surface modulation of the catalyst. They not only stabilize the higher oxidation state of Ni but also serve as a potential active site for OER. The presence of Fe impurity paves the way for the lattice oxygen mechanism boosting the O_2 production rate. This work leads to a deeper mechanistic understanding of the dynamics of Fe incorporation and helps in the development of catalysts with better performance.

Conflicts of interest

There are no conflicts to declare.

Acknowledgements

HC and CW acknowledge the funding from the International Max Planck Research School for Interface Controlled Materials for Energy Conversion (IMPRS-SurMat) and Max Planck Society for the support. HT thanks the Volkswagen Foundation (96_742) and the Carbon2Chem consortium funded by the

Bundesministerium für Bildung und Forschung (BMBF) and the Deutsche Forschungsgemeinschaft (DFG, German Research Foundation) Projektnummer 388390466–TRR 247 within the Collaborative Research Centre/Transregio 247 "Heterogeneous Oxidation Catalysis in the Liquid Phase" for the funding. We acknowledge DESY (Hamburg, Germany), a member of the Helmholtz Association HGF, for the provision of experimental facilities. Parts of this research were carried out at PETRA III, and we would like to thank PhD Alba San Jose Mendez for assistance in using beamline P02.1 (beamtime was allocated for proposal I-20210517). We would like to express our gratitude towards H. Petersen, P. Sharma, I. Kappel, and T. H. Ulucan for their support during *in situ* XRD beamtimes. We also thank H. Petersen, J. Ternieden, B. Florian, and E. Budiyanto for supporting microstructure analysis, XRD, ICP-OES, and electrocatalytic measurements.

References

1 H. Dau, C. Limberg, T. Reier, M. Risch, S. Roggan and P. Strasser, *ChemCatChem*, 2010, **2**, 724–761.
2 B. M. Hunter, H. B. Gray and A. M. Muller, *Chem. Rev.*, 2016, **116**, 14120–14136.
3 J. Rogelj, M. Schaeffer, M. Meinshausen, R. Knutti, J. Alcamo, K. Riahi and W. Hare, *Environ. Res. Lett.*, 2015, **10**, 105007.
4 Y. Lee, J. Suntivich, K. J. May, E. E. Perry and Y. Shao-Horn, *J. Phys. Chem. Lett.*, 2012, **3**, 399–404.
5 S. Park, Y. Shao, J. Liu and Y. Wang, *Energy Environ. Sci.*, 2012, **5**, 9331–9344.
6 J. T. Mefford, X. Rong, A. M. Abakumov, W. G. Hardin, S. Dai, A. M. Kolpak, K. P. Johnston and K. J. Stevenson, *Nat. Commun.*, 2016, **7**, 11053.
7 F. Song, L. Bai, A. Moysiadou, S. Lee, C. Hu, L. Liardet and X. Hu, *J. Am. Chem. Soc.*, 2018, **140**, 7748–7759.
8 H. Wang, J. Qi, N. Yang, W. Cui, J. Wang, Q. Li, Q. Zhang, X. Yu, L. Gu, J. Li, R. Yu, K. Huang, S. Song, S. Feng and D. Wang, *Angew Chem. Int. Ed. Engl.*, 2020, **59**, 19691–19695.
9 K. A. Stoerzinger, M. Risch, J. Suntivich, W. M. Lü, J. Zhou, M. D. Biegalski, H. M. Christen, Ariando, T. Venkatesan and Y. Shao-Horn, *Energy Environ. Sci.*, 2013, **6**, 1582–1588.
10 J. Du, T. Zhang, F. Cheng, W. Chu, Z. Wu and J. Chen, *Inorg. Chem.*, 2014, **53**, 9106–9114.
11 Z. Yan, H. Sun, X. Chen, X. Fu, C. Chen, F. Cheng and J. Chen, *Nano Res.*, 2018, **11**, 3282–3293.
12 A. Grimaud, K. J. May, C. E. Carlton, Y. L. Lee, M. Risch, W. T. Hong, J. Zhou and Y. Shao-Horn, *Nat. Commun.*, 2013, **4**, 2439.
13 K. J. May, C. E. Carlton, K. A. Stoerzinger, M. Risch, J. Suntivich, Y.-L. Lee, A. Grimaud and Y. Shao-Horn, *J. Phys. Chem. Lett.*, 2012, **3**, 3264–3270.
14 E. Fabbri, M. Nachtegaal, T. Binninger, X. Cheng, B. J. Kim, J. Durst, F. Bozza, T. Graule, R. Schaublin, L. Wiles, M. Pertoso, N. Danilovic, K. E. Ayers and T. J. Schmidt, *Nat. Mater.*, 2017, **16**, 925–931.
15 J.-W. Zhao, Z.-X. Shi, C.-F. Li, Q. Ren and G.-R. Li, *ACS Mater. Lett.*, 2021, **3**, 721–737.
16 A. Grimaud, O. Diaz-Morales, B. Han, W. T. Hong, Y. L. Lee, L. Giordano, K. A. Stoerzinger, M. T. M. Koper and Y. Shao-Horn, *Nat. Chem.*, 2017, **9**, 457–465.
17 C. Yang, M. Batuk, Q. Jacquet, G. Rousse, W. Yin, L. Zhang, J. Hadermann, A. M. Abakumov, G. Cibin, A. Chadwick, J.-M. Tarascon and A. Grimaud, *ACS Energy Lett.*, 2018, **3**, 2884–2890.
18 J. S. Yoo, X. Rong, Y. Liu and A. M. Kolpak, *ACS Catal.*, 2018, **8**, 4628–4636.
19 I. Spanos, J. Masa, A. Zeradjanin and R. Schlögl, *Catal. Lett.*, 2020, **151**, 1843–1856.
20 S. Anantharaj, S. Kundu and S. Noda, *Nano Energy*, 2021, **80**, 105514.
21 R. Subbaraman, N. Danilovic, P. P. Lopes, D. Tripkovic, D. Strmcnik, V. R. Stamenkovic and N. M. Markovic, *J. Phys. Chem. C*, 2012, **116**, 22231–22237.
22 L. Trotochaud, S. L. Young, J. K. Ranney and S. W. Boettcher, *J. Am. Chem. Soc.*, 2014, **136**, 6744–6753.
23 H. Li, Y. Chen, J. Ge, X. Liu, A. C. Fisher, M. P. Sherburne, J. W. Ager and Z. J. Xu, *JACS Au*, 2021, **1**, 108–115.
24 R. Zhang, P. E. Pearce, Y. Duan, N. Dubouis, T. Marchandier and A. Grimaud, *Chem. Mater.*, 2019, **31**, 8248–8259.
25 D. Y. Chung, P. P. Lopes, P. F. B. D. Martins, H. He, T. Kawaguchi, P. Zapol, H. You, D. Tripkovic, D. Strmcnik, Y. Zhu, S. Seifert, S. Lee, V. R. Stamenkovic and N. M. Markovic, *Nat. Energy*, 2020, **5**, 222–230.
26 D. Friebel, M. W. Louie, M. Bajdich, K. E. Sanwald, Y. Cai, A. M. Wise, M. J. Cheng, D. Sokaras, T. C. Weng, R. Alonso-Mori, R. C. Davis, J. R. Bargar, J. K. Norskov, A. Nilsson and A. T. Bell, *J. Am. Chem. Soc.*, 2015, **137**, 1305–1313.
27 S. Lee, L. Bai and X. Hu, *Angew Chem. Int. Ed. Engl.*, 2020, **59**, 8072–8077.
28 A. Coelho, *J. Appl. Crystallogr.*, 2018, **51**, 210–218.
29 P. Scardi and M. Leoni, *J. Appl. Crystallogr.*, 2006, **39**, 24–31.
30 P. Scardi, *Z. Kristallogr. - Cryst. Mater.*, 2002, **217**, 420–421.
31 P. Juhas, T. Davis, C. L. Farrow and S. J. L. Billinge, *J. Appl. Crystallogr.*, 2013, **46**, 560–566.
32 X. Yang, P. Juhas, C. L. Farrow and S. J. L. Billinge, *arXiv*, 2015, preprint, arXiv:1402.3163v3, DOI: **10.48550/arXiv.1402.3163**.
33 M. Vega-Paredes, R. Aymerich-Armengol, D. A. Esteban, S. Marti-Sanchez, S. Bals, C. Scheu and A. G. Manjon, *ACS Nano*, 2023, **17**, 16943–16951.
34 M. Vega-Paredes, C. Scheu and R. Aymerich-Armengol, *ACS Appl. Mater. Interfaces*, 2023, **15**, 46895–46901.
35 P. P. Lopes, D. Y. Chung, X. Rui, H. Zheng, H. He, P. F. B. D. Martins, D. Strmcnik, V. R. Stamenkovic, P. Zapol, J. F. Mitchell, R. F. Klie and N. M. Markovic, *J. Am. Chem. Soc.*, 2021, **143**, 2741–2750.
36 E. Budiyanto, S. Salamon, Y. Wang, H. Wende and H. Tuysuz, *JACS Au*, 2022, **2**, 697–710.
37 P. Bera, *Int. J. Self-Propag. High-Temp. Synth.*, 2019, **28**, 77–109.
38 S. J. Billinge and M. G. Kanatzidis, *Chem. Commun.*, 2004, 749–760, DOI: **10.1039/b309577k**.
39 B. Ingham, *Crystallogr. Rev.*, 2015, **21**, 229–303.

40 C. C. McCrory, S. Jung, J. C. Peters and T. F. Jaramillo, *J. Am. Chem. Soc.*, 2013, **135**, 16977–16987.
41 G. H. Moon, M. Yu, C. K. Chan and H. Tuysuz, *Angew Chem. Int. Ed. Engl.*, 2019, **58**, 3491–3495.
42 M. S. Burke, M. G. Kast, L. Trotochaud, A. M. Smith and S. W. Boettcher, *J. Am. Chem. Soc.*, 2015, **137**, 3638–3648.
43 M. W. Louie and A. T. Bell, *J. Am. Chem. Soc.*, 2013, **135**, 12329–12337.
44 A. Schober, J. Fowlie, M. Guennou, M. C. Weber, H. Zhao, J. Íñiguez, M. Gibert, J.-M. Triscone and J. Kreisel, *APL Mater.*, 2020, **8**, 061102.
45 O. Diaz-Morales, F. Calle-Vallejo, C. de Munck and M. T. M. Koper, *Chem. Sci.*, 2013, **4**, 2269–2696.
46 B. S. Yeo and A. T. Bell, *J. Phys. Chem. C*, 2012, **116**, 8394–8400.
47 B. J. Trzesniewski, O. Diaz-Morales, D. A. Vermaas, A. Longo, W. Bras, M. T. Koper and W. A. Smith, *J. Am. Chem. Soc.*, 2015, **137**, 15112–15121.
48 N. Biškup, J. Salafranca, V. Mehta, M. P. Oxley, Y. Suzuki, S. J. Pennycook, S. T. Pantelides and M. Varela, *Phys. Rev. Lett.*, 2014, **112**, 087202.
49 N. Gauquelin, E. Benckiser, M. K. Kinyanjui, M. Wu, Y. Lu, G. Christiani, G. Logvenov, H. U. Habermeier, U. Kaiser, B. Keimer and G. A. Botton, *Phys. Rev. B: Condens. Matter Mater. Phys.*, 2014, **90**, 195140.
50 S.-Y. Chen, A. Gloter, A. Zobelli, L. Wang, C.-H. Chen and C. Colliex, *Phys. Rev. B: Condens. Matter Mater. Phys.*, 2009, **79**, 104103.
51 X. Ren, C. Wei, Y. Sun, X. Liu, F. Meng, X. Meng, S. Sun, S. Xi, Y. Du, Z. Bi, G. Shang, A. C. Fisher, L. Gu and Z. J. Xu, *Adv. Mater.*, 2020, **32**, e2001292.
52 N. Li, D. K. Bediako, R. G. Hadt, D. Hayes, T. J. Kempa, F. von Cube, D. C. Bell, L. X. Chen and D. G. Nocera, *Proc. Natl. Acad. Sci. U. S. A.*, 2017, **114**, 1486–1491.
53 Y. Dou, C.-T. He, L. Zhang, M. Al-Mamun, H. Guo, W. Zhang, Q. Xia, J. Xu, L. Jiang, Y. Wang, P. Liu, X.-M. Chen, H. Yin and H. Zhao, *Cell Rep. Phys. Sci.*, 2020, **1**, 100077.
54 Y. Pan, X. Xu, Y. Zhong, L. Ge, Y. Chen, J. M. Veder, D. Guan, R. O'Hayre, M. Li, G. Wang, H. Wang, W. Zhou and Z. Shao, *Nat. Commun.*, 2020, **11**, 2002.
55 A. K. Tomar, U. N. Pan, N. H. Kim and J. H. Lee, *ACS Energy Lett.*, 2022, **8**, 565–573.